THE ASTROPHYSICAL JOURNAL, 482:143–155, 1997 June 10

X-RAY EMISSION FROM THE FORNAX CLUSTER

C. JONES, C. STERN, W. FORMAN, J. BREEN, L. DAVID, AND W. TUCKER
Harvard-Smithsonian Center for Astrophysics, 60 Garden Street, Cambridge, MA 02138

AND

M. FRANX
Kapteyn Astronomical Institute, University of Groningen, P.O. Box 800, 9700 AV Groningen, Netherlands
Received 1994 May 9; accepted 1996 December 17

ABSTRACT

We have analyzed the *ROSAT* PSPC observations of the central region of the Fornax cluster, a relatively poor group of galaxies at a distance of about 24 Mpc. The brightest X-ray and optical galaxy in the group is NGC 1399, an E1 galaxy located near the center of the Fornax cluster. We characterize the hot gas around the galaxy, derived from a $2'$ to $18'$ annulus around NGC 1399, as having a mean temperature of 1.30 ± 0.05 keV and a heavy element abundance of 0.6 ± 0.1 with respect to solar abundance ($\mathrm{Fe/H} = 4.68 \times 10^{-5}$ by number). Spatially resolved spectral data provide both gas temperature and gas abundance profiles extending to 125 kpc ($18'$) from the galaxy. The temperature distribution, combined with the X-ray surface brightness profile, yields an accurate determination of the gravitating mass within 125 kpc, which falls in the range $(4.3–8.1) \times 10^{12}\ M_\odot$ (95% confidence range, including systematic uncertainties). If we include the extended optical halo around NGC 1399, the mass-to-light ratio increases with radius from $33 \pm 8\ M_\odot/L_\odot$ at 18 kpc to $70 \pm 22\ M_\odot/L_\odot$ at 110 kpc. We compare the heavy element abundance distribution measured around NGC 1399 with that measured around the Virgo galaxy NGC 4472, as well as to models for hot coronae. We find that the abundance distribution is in good agreement with that previously measured for NGC 4472 by Forman et al. in 1993. For both galaxies, the observed abundance profiles require both a weak evolution of the type Ia supernova rate with time and a present epoch rate which agrees with that of Cappellaro et al.

We compare mass measurements in NGC 1399 to those for M87. The similarity of the optical masses in these systems and their differences in gas masses and gravitating masses lead us to suggest that the optical galaxies formed at an early stage when the central potentials of these two systems were similar. Subsequent infall of gas and dark matter into the larger, deeper Virgo potential resulted in the greater mass of the Virgo cluster compared to Fornax.

We also report on X-ray properties of thirteen other Fornax galaxies. Eight of these were detected in *ROSAT* images with luminosities in the 0.2 to 2 keV energy band from 1×10^{39} to 1.6×10^{41} ergs $\mathrm{s^{-1}}$. Five galaxies were sufficiently bright to permit spectral analyses and all but one (NGC 1380) had spectra consistent with thermal emission. Two (NGC 1404 and NGC 1387) of the four galaxies with well-constrained spectral parameters have hot coronae with characteristic gas temperatures of about 0.5 keV and iron abundances less than that found around NGC 1399 and other bright ellipticals. To maintain these hot coronae, the absolute magnitudes of these galaxies must be brighter than -19. Thus the distance to Fornax must be at least 18 Mpc, and, if there are no large peculiar velocities, the Hubble constant should be less than 75 km $\mathrm{s^{-1}\ Mpc^{-1}}$. Since these galaxies are all members of Fornax, distance uncertainties do not affect the relationship between their optical magnitude and X-ray luminosity. Analysis of the Fornax galaxies supports the contention that the scatter in the X-ray and optical relationship is intrinsic and does not arise solely from distance uncertainties. For the elliptical galaxy NGC 1404, the X-ray images show that the hot corona is distorted and likely is being stripped, indicating infall of the galaxy toward NGC 1399 and the cluster center.

Subject headings: galaxies: abundances — galaxies: elliptical and lenticular, cD — galaxies: individual: (NGC 1399) — galaxies: structure — X-rays: galaxies

1. INTRODUCTION

The first X-ray images of NGC 4406 (M86) in the Virgo cluster changed the widely held view that elliptical and S0 galaxies were gas-free systems (Forman et al. 1979). Subsequently, the discovery from *Einstein* observations that hot ($T \sim 10^7$ K) gaeous coronae were a common feature of bright E and S0 galaxies and the realization that the gas would be in hydrostatic equilibrium provided a new technique to address the gravitating mass distributions of these galaxies (Forman, Jones, & Tucker 1985; Fabian et al. 1986). In this paper we report the results of our analysis of two deep (54 ksec and 18 ksec) *ROSAT* PSPC observations of the central region of the Fornax cluster. In addition to measuring the gravitating mass, the *ROSAT* PSPC observations allow the measurement of the heavy element abundance of the hot gas around NGC 1399.

NGC 1399 is the brightest Fornax galaxy and is located near the center of the cluster. Classified as an E1 (de Vaucouleurs, de Vaucouleurs, & Corwin 1976), NGC 1399 has a very large globular cluster population (Hanes & Harris 1986; Bridges, Hanes, & Harris 1991) and an extensive stellar envelope characteristic of a cD galaxy (Schombert 1986). Parameters for NGC 1399 are given in Table 1. NGC 1399 was previously observed in X-rays with *EXOSAT* (Mason & Rosen 1985), the *Einstein* IPC (Thomas et al. 1986; Killeen & Bicknell 1988), *Ginga* (Ikebe et al. 1992) and

TABLE 1

OBSERVATIONAL PARAMETERS OF NGC 1399

Property	Adopted Value
Distance	24.0 Mpc
Blue magnitude	10.55
Velocity dispersion	310 km s^{-1}
Heliocentric velocity	1422 km s^{-1}
Group velocity	1411 km s^{-1}
X-ray luminosity within 100 kpc (0.2–2 keV)	4.2×10^{41} ergs s^{-1}

BBXRT (Serlemitsos et al. 1993). With the *Einstein* IPC observations, Killeen & Bicknell (1988) could obtain only one emission weighted temperature for the X-ray emission surrounding NGC 1399. Similarly, with *Ginga*, Ikebe et al. (1992) determined a single temperature. With BBXRT, Serlemitsos et al. measured the temperature in two regions, one on the galaxy center, where there is radiatively cooling gas, and one in an outer region 3′.5–8′.6 from the galaxy center. Rangarajan et al. (1995) made a detailed study of the central cooling region using 15 ksec of the *ROSAT* observation centered on NGC 1399 (the primary observation analyzed in this paper), which had a total exposure time of 54 ksec. Thus, in this paper, we do not address the central region in detail, but instead concentrate on the region outside the center of NGC 1399. Recently Ikebe et al. (1996) have analyzed the *Advanced Satellite for Cosmology and Astrophysics* (*ASCA*) images of NGC 1399. We compare the *ROSAT* and *ASCA* results.

Measurement of the gravitating mass depends on the temperature profile of the hot gas. By providing accurate, spatially resolved measurements of the gas temperature (as well as the surface brightness profile), the *ROSAT* PSPC observations provide a good determination of the gravitating mass distribution in this system. For NGC 1399, we can measure accurately the gas density and temperature to a radius of 18′, a radial distance of 125 kpc, assuming a distance modulus of 31.9 (equivalent to 24.0 Mpc; Ferguson 1989).

In the sections which follow, we first describe the details of analysis, including the determination of gas temperature and density distributions about NGC 1399 (§ 2). In § 3, we compute the gravitating mass and compare this value with that determined from the velocity dispersion of globular clusters. In § 4, we compare the radial distributions of the mass components—the gas mass, the stellar mass, and the dynamical mass—around NGC 1399 with M87 in the Virgo cluster. In § 5, we compare the abundance measurements to models which allow us to constrain the evolution of the type Ia supernova rate and its present epoch value. In § 6, we discuss the X-ray properties of other galaxies in the Fornax cluster.

2. THE *ROSAT* PSPC IMAGE OF NGC 1399

We obtained a deep pointed *ROSAT* PSPC observation centered on NGC 1399. The revised processing of the data provided a significantly longer exposure than the first standard analysis. The exposure time in the final processed image was 54 ksec spanning the interval 1991 August 15–16. We examined the counting rate in the image as a function of time and found intervals when the counting rate significantly exceeded the standard low background rate generally observed in the PSPC. We used the Snowden et al. (1992) techniques to remove these intervals of high background. This resulted in removing nearly half of the original time, yielding a low-background image containing 27.8 ksec. To ensure that the high-background times did not affect the spectral determinations, we used the low-background "cleaned" image for all succeeding analyses reported here. However, we also compared the analysis for the surface brightness profiles and galaxy luminosities obtained from the "cleaned" and the full observation and found consistent results.

Figure 1 shows an isointensity contour map of the X-ray emission over the energy band 0.2–2.2 keV after exposure map corrections were performed. The contour map is made using a "wavelet smoothing" algorithm which removes noise and allows detection of features of low surface brightness adjacent to bright point-like emission (see Vikhlinin, Forman, & Jones 1996 for details). In performing the exposure map correction, we generated a 512×512 exposure map following the prescription of Snowden et al. (1992), since we found that the exposure map generated by the standard processing system was not adequate to accurately flat-field the image. Figure 1 shows that the emission around NGC 1399 appears asymmetric. The optical galaxy NGC 1399 is offset from the center of the outer X-ray isophotes by about 6′, which corresponds to about 40 kpc for an assumed distance to NGC 1399 of 24 Mpc. Because of this asymmetry, we performed the spectral analysis and surface brightness modeling using azimuthal as well as radial binning.

2.1. *Spectral Analysis of the Gas around NGC 1399*

We used the spectral information from the PSPC to determine the emission weighted temperature in annuli and in azimuthal regions around NGC 1399. The data used in the fits were extracted from the image after excluding regions around other galaxies and point sources. Background was obtained in regions 40′ to 45′ from the field center (with sources excluded) and then corrected for telescope vignetting (emission weighted by distance off-axis) in each of the 34 pulse height channels before it was subtracted from the data in each source annulus. At a distance of 40′–45′ from the center of the image, no X-ray emission associated with NGC 1399 or the Fornax cluster was detected. Any residual cluster emission would be a small fraction of the background emission. To compare the source spectra to models of optically thin thermal radiation, we excluded the lowest and highest energy channels and fitted the energy range from 0.17 to 1.91 keV with spectral fitting software from XSPEC. Table 2 gives the parameters resulting from the spectral fits and shows the statistical precision possible with the PSPC for determining the temperatures around 1 keV. In these models, we used the 1993 January response for the PSPC and an iron abundance of 4.68×10^{-5} (by number). We also fitted these spectra using the 1992 March PSPC response and found that the best-fit temperature was reduced by a few percent, while the abundance was reduced by about 10%. Note that since the emission lines of iron dominate the spectrum at temperatures around 1 keV, the measured constraint on the heavy element abundance is actually for iron.

The radial distributions of the gas temperature, the iron abundance, and the column density from Table 2 are plotted in Figure 2. It is apparent that beyond the central cooling region, the gas temperature is nearly isothermal,

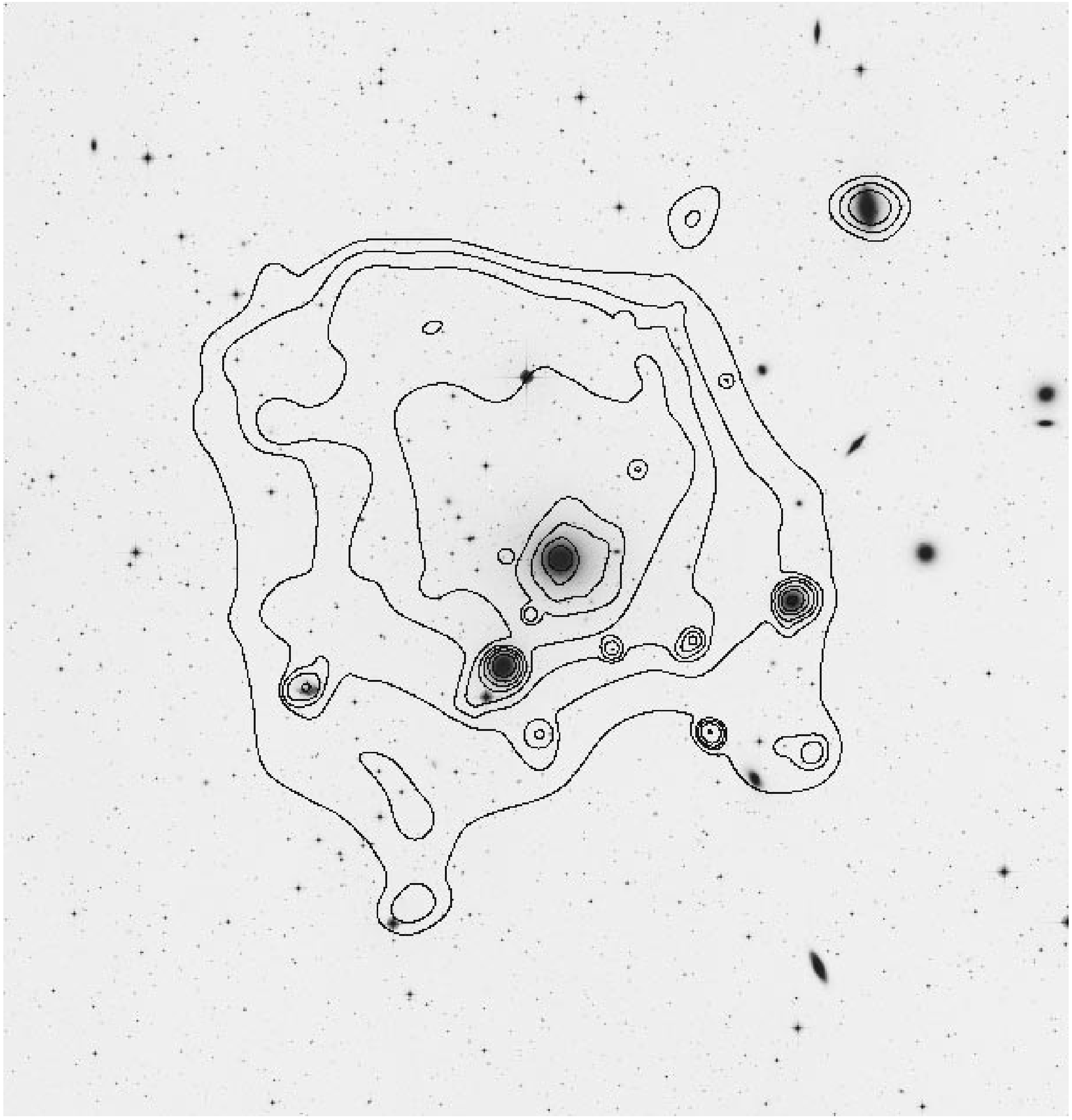

FIG. 1.—X-ray isointensity contours (0.42–1.31 keV) superposed on an optical image. The contours are generated from a Gaussian smoothed, exposure map corrected image. The image shows the presence of emission associated with individual galaxies as well as diffuse emission covering the core region of the Fornax cluster system.

varying by less than 0.1 keV over the full radial range from 30 to 125 kpc (4′ to 18′). Fitting the temperature profile in this region to a function of the form $T(r) = \alpha r + T_0$ yields best-fit parameters of $T_0 = 1.218 \pm 0.013$ keV and $\alpha = -0.0003 \pm 0.0002$. Alternatively, fitting a power law distribution, $T(r) = T(0)r^{\alpha}$, gives $T(0) = 1.27 \pm 0.04$ keV and $\alpha = -0.014 \pm 0.008$. Hence, outside the cooling region, α is consistent with zero for both fits; i.e., we have an isothermal temperature distribution. The fits to the above two functional forms are shown in Figure 3. In the inner region, the decrease in the gas temperature is characteristic of a cooling flow (Thomas et al. 1986). The gas within this region is most likely inhomogeneous, with gas at many different temperatures (see Fabian 1994 for a discussion of cooling flows and Rangarajan et al. 1995 for a detailed analysis of the spectral characteristics of this region.)

As Table 2 and Figure 2 show, we find no large changes in the hydrogen column density within the image. A χ^2 fit to a constant value for the column density in the seven outer radial bins (beyond 30 kpc) yields a mean value of 1.16×10^{20} atoms cm^{-2} and $\chi^2 = 11.0$, consistent with a constant value. The column density we measure with the PSPC is in good agreement with the galactic column density of 1.3×10^{20} cm^{-2} (Stark et al. 1992). We do not find the higher absorption in the central and outer regions of NGC 1399 that was reported by Serlemitsos et al. (1993) from BBXRT observations. Rangarajan et al. (1995), in their analysis of part of this *ROSAT* observation, found that a column density higher than Galactic is required in the central region if an additional soft component is included in the spectral fitting. As shown in Table 2 and Figure 3, as well as in Figures 3 and 4 of Rangarajan et al., the spectra do show cooler gas in the central 10 kpc region. Thus, single temperature spectral fits probably are not adequate to describe the core region.

The radial profile of the heavy element abundance is the third parameter measured from the spectral data and is formally consistent with a uniform distribution ($\chi^2 = 12.8$

TABLE 2

SPECTRAL PARAMETERS DETERMINED IN ANNULI AROUND NGC 1399

Annulus (arcmin)	Fitted Parameter	Best Fit	Confidence Ranges $\Delta\chi^2 = 1.0$	$\Delta\chi^2 = 2.71$	$\Delta\chi^2 = 4.61$	$\Delta\chi^2 = 6.25$
0–1	kT (keV)	0.88	0.87–0.89	0.87–0.90	0.87–0.90	0.86–0.91
0–1	$n_H(\times 10^{20})$	1.80	1.63–1.98	1.51–2.09	1.42–2.18	1.36–2.24
0–1	Abundance	0.44	0.38–0.50	0.35–0.55	0.33–0.59	0.32–0.62
1–2	kT (keV)	1.12	1.11–1.14	1.10–1.15	1.10–1.18	1.09–1.20
1–2	$n_H(\times 10^{20})$	0.96	0.80–1.14	0.70–1.26	0.63–1.36	0.59–1.43
1–2	Abundance	0.92	0.76–1.10	0.68–1.24	0.62–1.36	0.58–1.45
2–4	kT (keV)	1.32	1.30–1.36	1.28–1.37	1.26–1.39	1.25–1.39
2–4	$n_H(\times 10^{20})$	0.94	0.81–1.08	0.73–1.17	0.67–1.24	0.63–1.29
2–4	Abundance	1.30	1.12–1.53	1.01–1.70	0.94–1.84	0.89–1.95
4–6	kT (keV)	1.26	1.20–1.30	1.17–1.33	1.14–1.35	1.14–1.36
4–6	$n_H(\times 10^{20})$	1.29	1.14–1.44	1.04–1.54	0.97–1.62	0.92–1.67
4–6	Abundance	0.57	0.47–0.69	0.42–0.77	0.38–0.84	0.36–0.90
6–8	kT (keV)	1.30	1.25–1.35	1.21–1.37	1.18–1.39	1.16–1.41
6–8	$n_H(\times 10^{20})$	1.63	1.46–1.81	1.35–1.92	1.26–2.01	1.20–2.08
6–8	Abundance	0.47	0.38–0.57	0.34–0.65	0.30–0.72	0.28–0.77
8–10	kT (keV)	1.26	1.22–1.31	1.15–1.34	1.14–1.36	1.13–1.38
8–10	$n_H(\times 10^{20})$	1.49	1.28–1.70	1.15–1.83	1.05–1.94	0.98–2.01
8–10	Abundance	0.51	0.41–0.64	0.35–0.74	0.31–0.83	0.29–0.90
10–12......	kT (keV)	1.22	1.16–1.27	1.14–1.30	1.13–1.33	1.12–1.34
10–12......	$n_H(\times 10^{20})$	1.62	1.42–1.82	1.30–1.95	1.20–2.05	1.13–2.12
10–12......	Abundance	0.47	0.38–0.58	0.33–0.66	0.30–0.73	0.28–0.79
12–14......	kT (keV)	1.24	1.18–1.28	1.14–1.31	1.13–1.33	1.13–1.35
12–14......	$n_H(\times 10^{20})$	1.40	1.20–1.60	1.07–1.74	0.97–1.84	0.91–1.92
12–14......	Abundance	0.62	0.50–0.77	0.44–0.89	0.39–0.99	0.36–1.07
14–16......	kT (keV)	1.16	1.13–1.22	1.12–1.25	1.11–1.28	1.11–1.29
14–16......	$n_H(\times 10^{20})$	1.88	1.64–2.13	1.49–2.29	1.37–2.41	1.28–2.50
14–16......	Abundance	0.48	0.38–0.60	0.34–0.70	0.31–0.78	0.29–0.85
16–18......	kT (keV)	1.11	1.10–1.13	1.08–1.14	1.07–1.15	1.07–1.17
16–18......	$n_H(\times 10^{20})$	1.91	1.67–2.15	1.52–2.31	1.40–2.34	1.33–2.53
16–18......	Abundance	0.42	0.34–0.51	0.30–0.59	0.27–0.65	0.25–0.70

for 9 degrees of freedom) of about half the solar value ($[Fe/H]_\odot = 4.68 \times 10^{-5}$ by number) as a function of radius. The increase in the abundance with radius over the central 30 kpc (4′) region in Figure 2 may be the result of our modeling the cooling region with a single temperature spectrum.

Since there is an asymmetry in the surface brightness distribution, we divided the spectral data into four azimuthal regions with annuli from 2′ to 6′, 6′ to 12′, and 12′ to 18′ and searched for variations in these sectors. Figure 4 summarizes the results of spectral fits to the hydrogen column density, gas temperature, and iron abundance. There are no significant variations. Therefore, we can confidently treat the NGC 1399 gas beyond 2′ as an azimuthally uniform medium as long as we account for the surface brightness asymmetry that we discuss below.

Except for the differences in the absorption found in the BBXRT and *ROSAT* analysis, the *ROSAT* spectral results are in good agreement with previous observations. The temperature fits (see Fig. 3 and Table 2) agree well with the temperature of 1.18 (+0.05, −0.07) keV found from BBXRT observations for the outer region (Serlemitsos et al. 1993). This is consistent with the temperature measured by the *EXOSAT* ME and lies just below the range measured for the inner 7′ with the *Einstein* IPC (Killeen & Bicknell 1988). The measured hydrogen column densities (see Fig. 2 and Table 2) also agree with the value of 1.4×10^{20} cm^{-2} reported by Stark et al. (1992). The heavy element abundances found in the *ROSAT* analysis (see Fig. 2 and Table 2) are also consistent with the values of 0.23–0.49 determined by Serlemitsos et al. for a single temperature model (and also with the values of 0.19–0.81 for their two-temperature model).

We investigated the suggestion from the BBXRT observations of a possible hotter component in the gas due to emission from either hotter (e.g., binary) sources or from the Fornax cluster (Serlemitsos et al. 1993). We included a second component in the spectral model, for an annulus from 10′ to 14′ and again for a 6′ radius region located 10′ to the northeast of NGC 1399. We found no significant improvement in the goodness of fit and thus no evidence in the PSPC spectra of a second, hotter component. If we include a hotter thermal component with a fixed normalization in the spectral fitting, we can compare this model to the observations and compare the goodness of fit to a model with only one thermal component, thus placing limits on the contribution of a hotter component. As examples, we can limit (at the 95% confidence level) the emission of a 2.5 keV, a 3.0 keV, or a 6.0 keV component to be less than 25% of the emission of that from the dominant 1 keV gas in the *ROSAT* energy band. If we include a harder component in the spectrum, the best-fit temperature of the soft component decreases by 0.04 keV and the uncertainty in the temperature increases by less than 0.05 keV (for 90% confidence limits). While the temperature of the soft component is relatively unaffected by a hard component, includ-

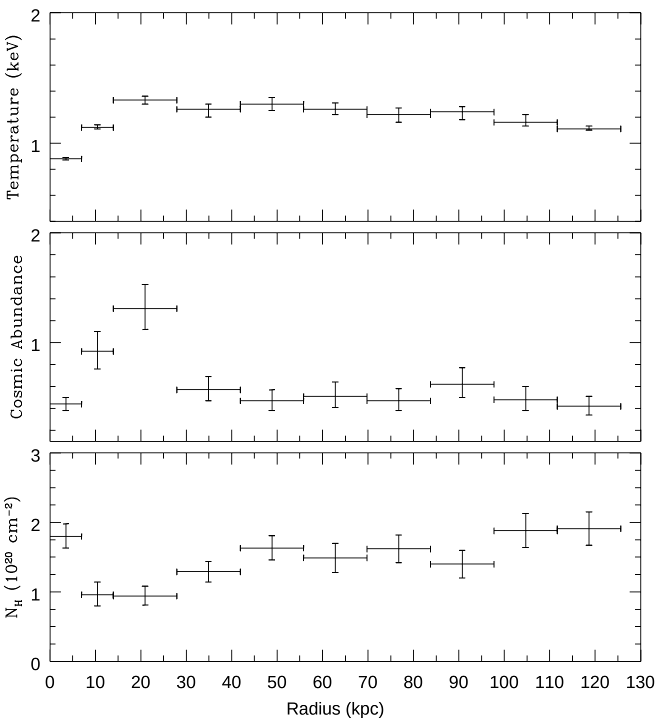

FIG. 2.—Gas temperature radial distribution from the center of NGC 1399, as well as heavy element abundance, and hydrogen column density as determined from *ROSAT* PSPC spectral fitting. The hydrogen column density is constant over the system and falls near the galactic value of 1.4×10^{20} cm^{-2} determined by Stark et al. (1992).

ing a hard component increases the best-fit heavy element abundance and its uncertainty by 0.1 of solar abundance and increases the best-fit column density by 1×10^{19} cm^2 and its uncertainty by 0.5×10^{19} cm^2.

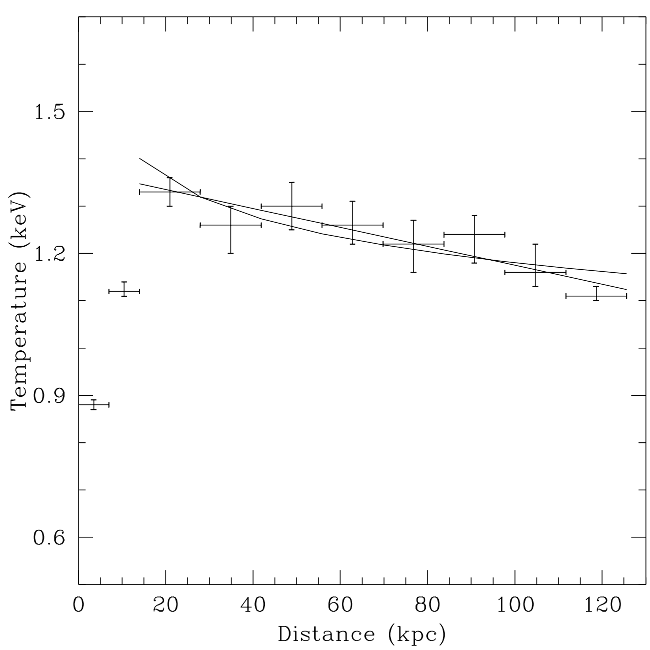

FIG. 3.—The radial gas temperature profile shows the cooler gas temperature within the central 2′ of NGC 1399 and the isothermal gas temperature extending to 18′ (125 kpc). Error bars are 1 σ ($\Delta\chi^2 = 1$) with all parameters free to vary (i.e., when determining the error on each of the parameters, the hydrogen column density, abundance, gas temperature, and normalization are all varied as free parameters).

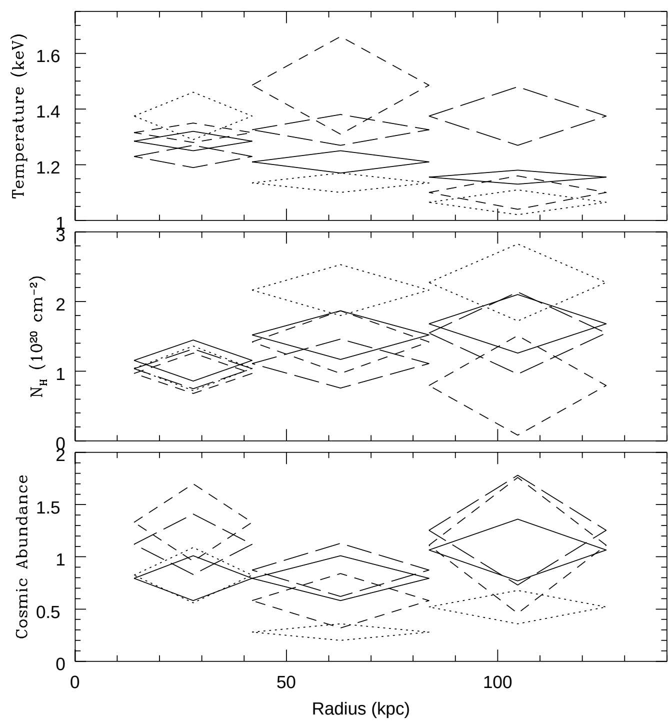

FIG. 4.—Parameters for NGC 1399 determined from the fits to the radially and azimuthally binned spectral data (given in Table 3). The parameters for the quadrant to the north are shown as solid lines, for the southern quadrant as dotted lines, as short-dashed lines for the eastern quadrant, and as long-dashed lines for the western quadrant. The top graph shows the gas temperature results, the middle graph the hydrogen column density, and the bottom graph the iron abundance.

Finally, to better compare the *ROSAT* spectra with those from BBXRT and *ASCA*, we also fitted spectra obtained for different regions in the PSPC image without first omitting the individual X-ray sources. For spectra beyond the central cooling region, we find that a two-component thermal spectral fit does provide a better description than a single component, with the second component having a temperature of $\approx$2–3 keV. For example, for the annulus from 3.′5 to 10′ from NGC 1399, if we take the first temperature component to be 1.1 keV, the best-fit temperature for the second component is 2.9 keV if we fit only the spectral energy bins above 1 keV, or 2.0 keV if we fit the lower energy channels as well. Thus, if the individual sources are not excluded from the spectral analysis, as they could not be with the limited spatial resolution of the BBXRT and *ASCA* observations, we do find a harder component in the entire spectrum. However, as discussed above, when these sources are excluded, we can constrain the presence of any hard component associated with the diffuse gas.

In summary, the results of our spectral analysis for NGC 1399 are that outside the central cooling region, the gas is essentially isothermal, the iron abundance is significantly less than solar, and the hydrogen column density is uniform and consistent with the galactic value.

2.2. *Gas Density Distribution*

To determine the gravitating mass distribution, it is necessary to derive the gas density distribution as well as the gas temperature profile. As shown in the previous section, the gas temperature is essentially isothermal, which allows a direct determination of the gas density distribution from the observed X-ray surface brightness distribution.

For isothermal gas, a surface brightness distribution characterized by a power law, $S(r) \propto r^{-\gamma}$, directly yields a gas density distribution given by $n_{gas} \propto r^{-\tau}$ with $\tau = (\gamma + 1)/2$.

We have analyzed the X-ray emission around NGC 1399 in a variety of ways to determine the surface brightness distribution and the uncertainty arising from the observed asymmetry (see Figure 1). At large radii there is an excess of emission to the northeast of NGC 1399, while at smaller radii there is greater emission southwest of the galaxy. We extracted the surface brightness profile in different azimuths and using different centers. Figure 5 shows the radial profile of the source extracted over two separate profiles for azimuthal angles 135°–315° and 315°–135° (with angles measured from north to east). We also generated a radial profile using a center determined by the outer contours and omitted the central 4′ region around NGC 1399. For each profile, we fit the surface brightness from 5′ to 18′ with a power law. The resulting exponents, τ, of the gas density distribution are 0.97 ± 0.04 and 1.27 ± 0.06 for the north-east and south-west regions, and 1.14 ± 0.06 for the third profile defined above that excludes NGC 1399. If we fit these profiles from 5′ to 40′, the best fitting exponents are 1.29 ± 0.05, 1.21 ± 0.06, and 1.32 ± 0.06. Differences in the radial profiles exist (the maximum difference in the exponent of the surface brightness distributions is 3.6 σ), but for the purposes of this paper, in which we are focusing on the determination of the gravitating mass, we need only know the measurement of the logarithmic derivative of the gas density distribution (derived from the surface brightness profiles), which differs by less than 15% over the radial range from 35 to 280 kpc (5′ to 40′). Beyond 280 kpc, the surface brightness falls below the extrapolation of the single–power-law description. We limit our mass determination to within 125 kpc, where the gas temperature is well-determined.

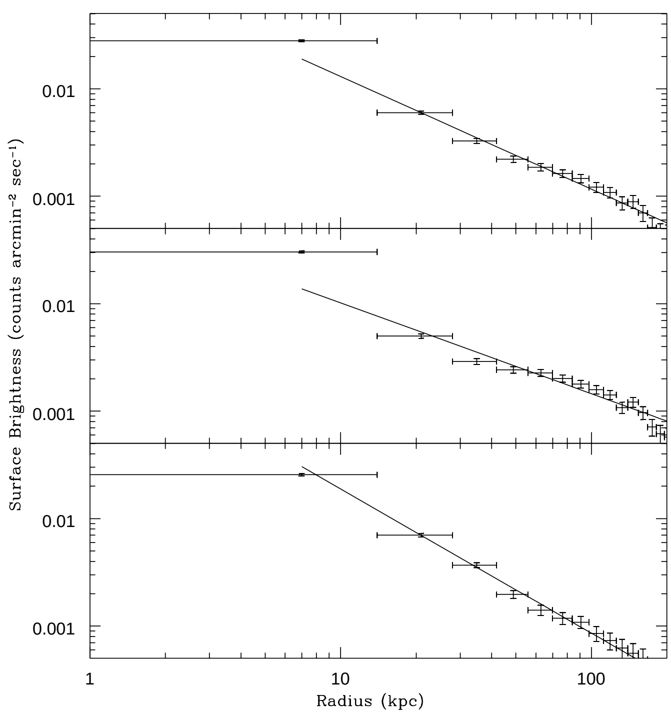

FIG. 5.—Surface brightness profile derived for three azimuthal regions centered on NGC 1399. The three curves are for the azimuthal region from 0°–360°, 135°–315°, and 315°–135° (with angles measured from north to east). All sources (except the emission around NGC 1399) were omitted in generating the surface brightness profiles. The profiles yield power laws whose exponents differ by less than 15%. Since the power-law exponent is the parameter used to determine the gravitating mass (see eq. [1]), the small variations in the surface brightness distribution do not significantly affect the gravitating mass measurement.

The maximum change in the counting rate in the 40′ to 45′ annular region that we used for background was 7%, which corresponds to 2% of the source flux at 16′ from NGC 1399. Since these background changes were small compared to the source flux and since we average over these changes, they do not significantly change the surface brightness distribution. Although we performed this analysis on the low-background PSPC image, the shape of the surface brightness profile from the full image gives a very similar gas density distribution.

While the determination of the gravitating mass depends only on the logarithmic derivative of the gas density profile (see eq. [2]), measuring the gas mass requires more detailed modeling and the determination of the central gas density. To determine the central gas density and the gas mass, we assumed an expression of the form

$$S(r) = S(0)[1 + (r/a)^2]^{-3\beta + 1/2} , \quad (1)$$

which has been used extensively to fit X-ray galaxy and cluster surface brightness distributions. For a range of a and β, we convolved each model with the PSPC point response function. The central 1′ region has a higher surface brightness than would be expected from the best-fit models determined outside this region. Because of the cooler gas temperature, we suggest that this enhanced emission is due to a central cooling flow, although the possibility of some X-ray emission from a low-luminosity active galactic nucleus in NGC 1399 cannot be excluded (however, note that Rangarajan et al. 1995 obtain a limit on the emission from a central point source of 4.6×10^{40} ergs s^{-1}). Earlier X-ray observations have shown that cooling flows and similar "central excesses" in the surface brightness are common in clusters of galaxies (e.g., Fabian, Nulsen & Canizares 1984, 1991; Jones & Forman 1984) with smaller cooling flows expected around individual early-type galaxies (e.g., Thomas et al. 1986). We used the best-fit parameters of this analysis for NGC 1399 ($a = 45''$ and $\beta = 0.35$) combined with the measured flux to determine the central gas density. We find a central hydrogen density of 0.018 cm^{-3}, which implies a central cooling time of just less than 10^9 years. With this parameterization of the gas density, we can compute the gas mass as a function of radius for comparison with the stellar mass distribution and the gravitating mass distribution. The gas mass within a 100 kpc radius is $1.66 \times 10^{11}\ M_\odot$.

If we scale the results of the *ASCA* analysis (Ikebe et al. 1996) for the distance we have adopted for NGC 1399, we find that the two determinations for the total gas mass are in good agreement. In particular, within a 100 kpc radius, Ikebe et al. measure a total gas mass of $1.54 \times 10^{11}\ M_\odot$, of which they attribute $6.6 \times 10^{10}\ M_\odot$ to the galaxy and $8.8 \times 10^{10}\ M_\odot$ to the cluster. This compares well with our determination of $1.66 \times 10^{11}\ M_\odot$.

3. MEASUREMENTS OF THE GRAVITATING MASS

The *ROSAT* PSPC images and spectral data allow us to determine the gas properties over the inner 125 kpc (approximately 18′) from NGC 1399. These measurements enable us to determine the gravitating mass for comparison with other luminous baryonic components as a function of radius.

Determination of the total mass distribution from measurements of the temperature and density distributions is basically straightforward and relies on few assumptions, all of which can be well-justified. The technique was first applied by Bahcall & Sarazin (1977) and Mathews (1978) to the X-ray emission surrounding M87. With *Einstein* IPC images, it also was used by Fabricant, Lecar, & Gorenstein (1980) and Fabricant & Gorenstein (1983) for M87, by Matilsky, Jones, & Foreman (1985) for NGC 4696 in the Centaurus cluster, by Forman et al. (1985) for NGC 4472, and by Mushotzky et al. (1994) for NGC 4636 to measure large mass-to-light ratios around those galaxies.

The hydrostatic equation can be combined with the ideal gas law for spherically symmetric systems to yield the gravitating mass within a radius r,

$$M_{\rm grav}(<r) = \frac{-kT(r)}{G\mu m_p}\left(\frac{d\ln\rho}{d\ln r} + \frac{d\ln T}{d\ln r}\right)r \qquad (2)$$

where μ = the mean molecular weight, m_p = the hydrogen mass, k = Boltzmann's constant, and $T(r)$ is the gas temperature at a radius r. Therefore, by measuring the gas density and temperature profiles from the X-ray observations, one can determine the total gravitating mass.

The determination of the gravitating mass using X-ray observations assumes that the X-ray emitting gas is in hydrostatic equilibrium with the underlying gravitational potential. Quantitatively, the requirement for the application of the hydrostatic assumption is that any gas flow velocities should be small compared to the speed of sound in the gas. As was emphasized in the first papers on hot coronae (e.g., Fabian et al. 1986; Forman et al. 1985), if the gas were not in hydrostatic equilibrium, but were being expelled in a wind with a velocity sufficiently large to invalidate the hydrostatic equation, then the gas replenishment rate would be up to 100 times higher than that predicted from standard stellar evolution. Furthermore, since the bulk of the gas mass lies at large radii, large flow velocities, even if only at large radii, still require unreasonably high replenishment rates.

The asymmetries in the X-ray emission suggest that the optical core of NGC 1399 may not be at rest, but may be moving slowly in a larger potential. As Figure 1 illustrates, the galaxy is offset from the center of the outer X-ray isophotes by about 6′, which corresponds to about 40 kpc for a distance to NGC 1399 of 24 Mpc. Similar offsets of the central galaxies from their X-ray emission have been reported by David et al. (1994) for NGC 5044, which is the central galaxy in a compact group, and for NGC 4472 in the Virgo cluster (Forman et al. 1993). David et al. suggested that the NGC 5044 galaxy could be in motion with respect to the surrounding dark matter. For NGC 1399, a very modest velocity of only 40 km s^{-1} is required to produce a motion of 40 kpc in 10^9 years, roughly the cooling time of the gas at a distance of 10 kpc from the galaxy center. Gravitational interactions with other bright galaxies in the central region of Fornax could produce such a velocity.

To derive the gravitating mass around NGC 1399, we restricted ourselves to the region beyond 4′, where both the surface brightness distribution and temperature profile are well-described by power laws. Within the central 4′ region, the gas temperature is lower than the outer regions. As Rangarajan et al. (1995) showed, the cooling time in this region is short compared to a Hubble time, so the cooler gas temperature probably results from the radiatively cooling gas. In the previous section, we derived power-law expressions for the gas density and gas temperature distributions. These can be inserted into equation (2) to yield

$$M_{\rm grav}(<r) = \frac{kT(r)}{G\mu m_p}(\tau - \alpha)r \qquad (3)$$

where r is the radius inside which we determine the gravitating mass and τ and α are the exponents describing the power-law distributions of the gas density and gas temperature. If we take the distance to NGC 1399 to be 24 Mpc, equation (3) becomes $M(<r) = 3.68 \times 10^{10}\, T_{\rm keV}(\tau - \alpha) r_{\rm kpc} M_{\odot}$. Note that $M(<r)$ scales linearly with the assumed distance to NGC 1399. The total mass within a given radius is plotted in Figure 6 as a function of the distance from the center of NGC 1399.

Grillmair et al. (1994) measured the velocity dispersion of globular clusters within 9′ of the core of NGC 1399 to be 388 ± 54 km s^{-1}. For an isotropic and isothermal velocity distribution, the estimated mass within 9′ (63 kpc) is $5.4 \times 10^{12}\, M_{\odot}$, nearly twice the mass implied by the X-ray observations. Although uncertainties alone can account for much of the difference in mass estimates, this difference suggests that the velocities of the globular clusters may be anisotropic.

The stellar light, and corresponding mass, of the galaxy and its highly extended envelope (Schombert 1986) can be compared to the gravitating mass. The stellar light profile is derived by combining the photometry of Franx (1988) for the inner 100″ with that of Schombert (1986) for the outer regions. The Schombert data are renormalized as pre-

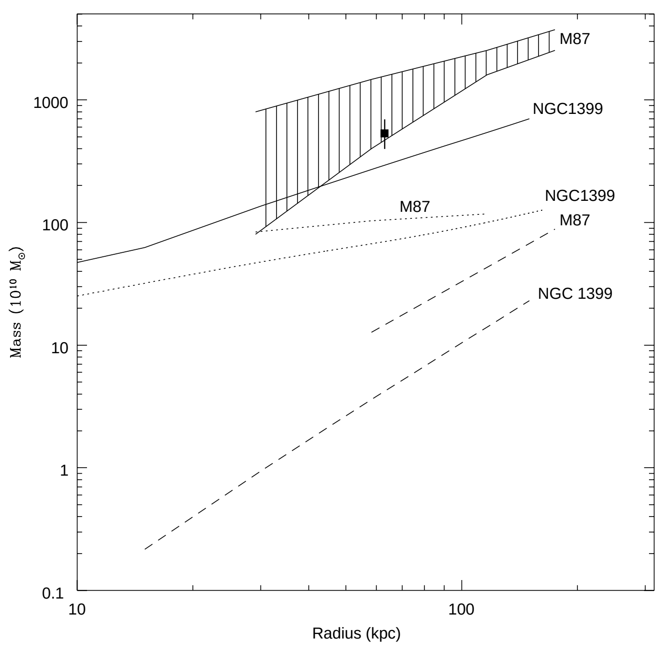

FIG. 6.—Radial distribution of the mass components around NGC 1399, including the gas mass seen in X-rays (*long-dashed line*), the stellar mass in galaxies (assuming an average $M/L = 8$, *dotted line*), and the gravitating mass derived from the X-ray data (*solid line*). For comparison, we also show these mass distributions around M87. The solid square marks the mass estimate derived by Grillmair et al. (1994) from the globular cluster velocity distribution.

scribed by Killeen & Bicknell (1988) to provide agreement over the full radial range. The resulting blue light profile is used with the X-ray–derived gravitating mass distribution to calculate the mass-to-light ratio.

In Figure 6 we show the three mass distributions—gas, stellar, and gravitating—which can be measured around NGC 1399. Within a 125 kpc radius, the gas mass is a relatively insignificant contributor to the total mass (less than 5% of the total). To compute the mass corresponding to the optical light, we assume a mass-to-light ratio of 8, appropriate to old stellar populations. The optically luminous matter contributes substantially to the total mass at small radii. Due to the extended optical envelope (Schombert 1986), the "optical mass" remains significant at large radii, decreasing to 20% of the gravitating mass within 125 kpc. The galaxy core with an absolute blue magnitude of $M_B = -21.35$ (from Franx 1988, scaled to a distance of 24 Mpc) represents slightly less than 40% of the total optical luminosity. Hence, the diffuse envelope dominates the light from the inner 125 kpc region surrounding NGC 1399.

In Figure 7, we use the blue light profile with the gravitating mass distribution derived from the X-ray observations to calculate the blue mass-to-light ratios. These mass-to-light ratios are computed in annuli and represent the mass-to-light ratio at the radii shown in Figure 7. The mass-to-light ratio increases with radius. Taking into account the uncertainties in the gas temperature and radial distribution and the uncertainties in the gas density distribution, we find a mass-to-light ratio of $33 \pm 8\ M_{\odot}/L_{\odot}$ at 18 kpc, which increases to $70 \pm 22\ M_{\odot}/L_{\odot}$ at 110 kpc. The mass-to-light ratios shown in Figure 7 are in good agreement with those determined by Serlemitsos et al. (1993), who used the *Einstein* IPC surface brightness profile and assumed the gas was isothermal.

Figure 7 shows that outside the galaxy core, where the mass-to-light ratio is about 6–8 $M_{\odot}/L_{\odot}$ (Killeen & Bicknell 1988), the mass-to-light ratio climbs quickly to larger values and then increases only slowly in the outer halo. Although the uncertainty in the mass-to-light ratio depends, in part, on the measured optical profile (Schombert 1986), it is of interest that the mass-to-light ratio measured in the outer regions approaches the "universal" value of ∼100–150 found for groups and rich clusters (David, Jones, & Forman 1995). This similarity suggests the dark matter in galaxy halos may be the same as the dark matter in groups and clusters.

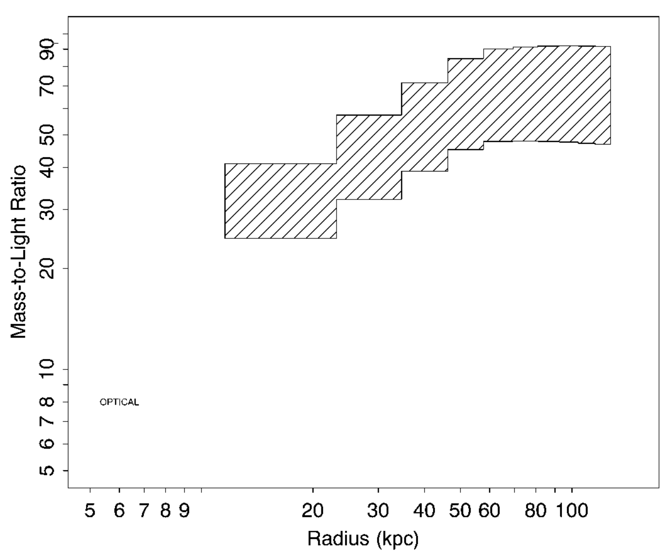

FIG. 7.—Mass-to-light ratio as a function of radius. The light is derived as described in the text and is in the blue band. Note the rise in mass-to-light ratio with increasing radius. The band indicates the range of gravitating mass allowed by the X-ray measurements.

4. NGC 1399 AND M87

To better understand NGC 1399 and the Fornax system, we compared the mass distributions described above to those measured in the M87/Virgo system. Figure 6, therefore, also shows the gravitating mass, optically luminous mass, and gas mass for M87. For M87 we used the masses given in Table 5 of Fabricant & Gorenstein (1983), but scaled those values to an assumed distance for M87 of 20 Mpc.

As Figure 6 shows, at large radii (around 100 kpc), the mass of the optically luminous matter around M87 is very similar to that surrounding NGC 1399. The profile for the optically luminous mass around NGC 1399 appears remarkably similar to that observed around M87. However, the measurement of faint optical extended envelopes is difficult over such large angular scales and is uncertain. Although the optically luminous matter distributions are quite similar, the distributions of total mass and gas mass in the two systems differ significantly, with M87 having roughly three times more mass in both gas and gravitating mass than NGC 1399 at about 100 kpc. This large difference in gas mass accounts for much of the difference in X-ray luminosity between these two systems.

Although the gas and gravitating masses of M87 and NGC 1399 differ considerably, the ratio of gas to gravitating mass is comparable. Both M87 and NGC 1399 have a ratio of gas to gravitating mass of about 2% at 100 kpc. This similarity is remarkable, considering that most of the luminous baryonic matter is found in the optically luminous stellar component and the ratio of gas to stellar mass varies so widely between the two systems (25% of the luminous baryons lie in gas in M87, while 6% of the luminous baryons are found in gas in NGC 1399).

The similarity of the optical masses for NGC 1399 and M87 and the differences between their total masses and the gas masses in these systems lead us to speculate that the galaxies may have formed through similar mechanisms at a relatively early stage in the formation of the surrounding cluster, when the central potentials were similar. Over time, the greater underlying density perturbation in Virgo produced a deeper potential around M87 containing both more gas and more total mass than in the shallower potential around NGC 1399. In both systems, as the potential deepened, the gas, becoming hotter, no longer contributed significantly to the growth of the galaxies, so that the optical masses of M87 and NGC 1399 remained at their early values. Thus the optical mass of the central galaxy in a group or cluster is not a good estimator of the total mass of the system.

5. IMPLICATIONS OF THE MEASURED HEAVY ELEMENT ABUNDANCE AROUND NGC 1399

The heavy element abundances in the hot coronae are determined by the supernova yields of heavy elements, the initial mass functions which govern the frequency with which supernova progenitors are formed, and the mass fraction of primordial gas remaining after galaxy formation. The heavy elements seen at present in the hot coronae of early-type galaxies arise from two sources—stellar mass loss from evolving stars and ejecta from type Ia supernovae, which are the predominant type of supernova observed in elliptical galaxies. Because the gas shed by stars and ejected by supernovae resides for long periods of time in the hot corona, radial abundance measurements can provide estimates of the supernova rate and its temporal evolution. In particular, radial abundance measurements can distinguish between scenarios for the origin of type Ia progenitor stars such as those proposed by Ciotti et al. (1991), which imply a rapid decline in the supernova rate with time compared to those used by Loewenstein & Mathews (1987) and David, Forman, & Jones (1990), who derived a considerably weaker dependence of the supernova rate on time.

A theoretical study of the dependence of the heavy element abundances on the supernova rate was made by Loewenstein & Mathews (1991). They characterized the time dependence of the type Ia supernova rate and the value of the rate at the present epoch as $R_{SN} = 2.2f(t/t_H)^{-s}$, where R_{SN} is the number of type Ia supernovae per 100 years per $10^{11}\ L_\odot$, t_H is the present time, f is the ratio of the present epoch supernova rate to that given by Tammann (1974), and s parameterizes the dependence of the supernova rate on time. Although, as our referee noted, these models were generated for King models, which are poor representations of the optical profile for NGC 1399, the Loewenstein & Mathews (1991) calculations remain the best currently available. In Figure 8, we superpose several of the model calculations of the radial behavior of the heavy element abundance for galaxy models of a $10^{11}\ L_\odot$ galaxy with a heavy halo. Along with the models we show the abundance measurements derived from the NGC 1399 observations presented here (Table 2) and from the *ROSAT* NGC 4472 observations (Forman et al. 1993). A luminosity of $10^{11}\ L_\odot$ is appropriate to NGC 1399, since its luminosity ranges from $(0.5\text{–}1.5) \times 10^{11}\ L_\odot$ for the preferred distance and the radius to which the optical light is integrated.

As shown in Figure 8, the abundance of heavy elements found in NGC 1399, which is less than solar abundance over a wide range of radii, is similar to that observed in NGC 4472 (Forman et al. 1993). Note that for this comparison the iron abundances are derived for $\mathrm{Fe/H} = 3.16 \times 10^{-5}$ (by number) and that the value of Fe/H (4.68×10^{-5}) presently incorporated in the XSPEC software would reduce the abundances shown in this figure by about 30%. (The values in Table 2 were derived for $\mathrm{Fe/H} = 4.68 \times 10^{-5}$.) The observed abundances eliminate models which require heavy element abundances much in excess of the solar value. In particular, the models proposed by D'Ercole et al. (1989; see also Ciotti et al. 1991) to explain the large range in X-ray luminosity for galaxies with similar optical luminosity predict iron abundances considerably in excess of solar abundances. Such high abundances conflict with the observations.

As is apparent from Figure 8, models with supernova rates that are higher at earlier epochs are inconsistent with the NGC 4472 and NGC 1399 observations. In particular, models in which the supernova rate is characterized by $s \geq 1.5$ predict heavy element abundances greater than observed. The models which adequately describe the observations have constant or slowly varying supernova rates ($|s| < 1$) and require relatively modest values of the

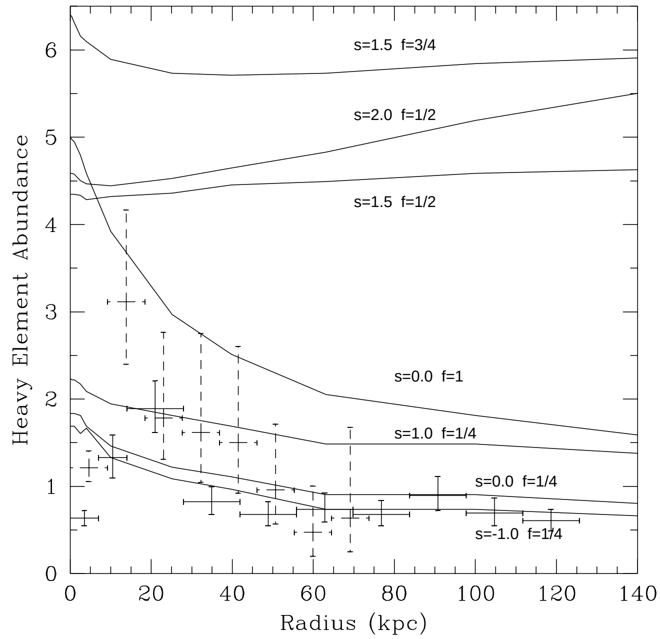

FIG. 8.—Abundance distribution around NGC 1399 compared to that around NGC 4472 (Forman et al. 1993) and model calculations (Loewenstein & Mathews 1991). The NGC 1399 measurements are shown as solid lines, while those for NGC 4472 are shown as dashed lines. The values for the iron abundance and its constancy throughout the corona for both NGC 1399 and NGC 4472 suggest a relatively constant supernova rate over time, with a present epoch value at the low end of the range derived by van den Bergh & Tammann (1991). Recent work by Worthey, Faber, & Jesus Gonzalez (1992) has shown that, compared to magnesium, iron is, on average, underabundant by a factor of 1.6–2.0 in the stellar component of giant elliptical galaxies. This fact would reduce the iron abundances shown in the model curves of Figure 1 but would not affect our conclusions about which models are appropriate.

present epoch supernova rate. In particular, for the models with $s = 0$, the model with present epoch supernova values equal to Tammann's (1974) rate ($f \approx 1$) produces iron abundances greater than observed, while the model with $f = \frac{1}{4}$ gives iron abundances in good agreement with the observations. Thus, for models of elliptical galaxies with heavy halos, the observations suggest a constant or slowly varying supernova rate ($|s| < 1$) and a present epoch supernova rate significantly less than $f = 1$. This supernova rate is consistent with the lower range of values derived by van den Bergh & Tammann (1991) and in agreement with the values derived by Cappellaro et al. (1993). Higher supernova rates are possible if the iron yields from type Ia supernovae are reduced of if the ejecta are not completely mixed into the hot ISM before cooling.

6. X-RAY EMISSION FROM GALAXIES IN FORNAX

We used our *ROSAT* image centered on NGC 1399 and an 18 ksec *ROSAT* PSPC image centered on NGC 1380 (obtained from the archive) to measure the X-ray luminosities and spectral properties for bright galaxies in the Fornax cluster. As summarized in Table 3, of the 13 NGC galaxies which lie in unobscured regions of these images, eight are detected in X-rays.

We fitted the PSPC spectral data for five of the brighter galaxies. Due to the emission from NGC 1399, which produces a varying background for the galaxies, we selected background regions near each galaxy. The parameters derived from the spectral analysis are given in Table 4.

TABLE 3

X-RAY EMISSION FROM GALAXIES IN FORNAX

Galaxy	R.A. (2000)	Decl. (2000)	Count Rate (Error)	L_X (ergs s^{-1})	Magnitude[a]	Type[b]
NGC 1374........	$3^h35^m18^s.5$	−35°13′44″	0.0037 (0.0009)	2.3×10^{39}	−19.89	E0
NGC 1375........	3 35 15.9	−35 17 13	0.0014 (0.0008)	$<1.6 \times 10^{39}$	−18.81	S0
NGC 1379........	3 36 02.2	−35 26 48	0.0054 (0.0013)	3.5×10^{39}	−20.03	E0
NCG1380	3 36 27.4	−34 58 19	0.0188 (0.0015)	1.1×10^{40}	−20.98	S0/Sa
NGC 1380A......	3 36 49.7	−34 43 21	0.0000 (0.0010)	$<1.9 \times 10^{39}$	−18.56	Spiral
NGC 1381........	3 36 33.1	−35 17 50	0.0014 (0.0008)	$<1.4 \times 10^{39}$	−19.44	S0(10)
NGC 1382........	3 36 58.0	−35 11 06	0.0010 (0.0010)	$<2.0 \times 10^{39}$	−18.09	E
NGC 1386........	3 36 54.3	−36 00 51	0.0146 (0.0018)	9.3×10^{39}	−19.78	Sa
NGC 1387........	3 36 57.3	−35 30 21	0.0413 (0.0016)	2.6×10^{40}	−20.20	SB0
NGC 1389........	3 37 02.0	−35 45 51	0.0014 (0.0006)	$<1.1 \times 10^{39}$	−19.46	S0/SB0
NGC 1404........	3 38 51.6	−35 35 38	0.2593 (0.0036)	1.6×10^{41}	−20.92	E2
NGC 1427........	3 42 07.8	−35 24 11	0.0126 (0.0019)	8.0×10^{39}	−20.09	E5
NGC 1427A......	3 40 12.8	−35 37 35	0.0143 (0.0013)	9.1×10^{39}	−18.63	Irr

[a] Absolute blue magnitudes were computed assuming a distance modulus of 31.9.

[b] Galaxy types are from Sandage & Tammann 1981, de Vaucouleurs & de Vaucouleurs 1964, and Sulentic & Tifft 1973.

Optically thin thermal emission is adequate to model all but the spectrum of the Sa galaxy NGC 1380. Its X-ray emission is better characterized by a steep, absorbed power law, probably from a compact source at the galaxy nucleus. For NGC 1404 and NGC 1387, the spectra can be modeled as emission from a single-temperature thermal gas with a well-constrained temperature of 0.5–0.6 keV. The temperature for NGC 1404 is consistent with that found from *ASCA* observations (Loewenstein et al. 1994). Gas temperatures for the early-type galaxies NGC 1379 and NGC 1381 would be consistent at 0.5 keV, although their temperatures are not well-constrained. These temperatures are substantially less than that measured for NGC 1399 and other X-ray bright ellipticals (e.g., NGC 4472, Forman et al. 1993; NGC 4636, Mushotzky et al. 1994). Although the X-ray emission from these galaxies is spatially extended, the low X-ray fluxes make it difficult to determine the temperature distribution with *ROSAT*, i.e., to map the mass distribution. However, if the galaxies' gas density distributions are similar to those of bright ellipticals, their lower gas temperatures indicate total masses less than half those of the bright, hot ellipticals at comparable radii.

For three of the early-type galaxies we constrain the heavy element abundances to be less than half the solar value. For NGC 1404, our metallicity determination of 0.16 relative to solar abundance is in excellent agreement with the *ASCA* measurement of 0.14 ± 0.03 (Loewenstein et al. 1994). The Fornax galaxies follow the general trend of having lower abundances for lower ISM gas temperatures (see Figure 5 of Jones & Forman 1994). Loewenstein et al. suggest that the low abundances in NGC 1404 and the Virgo galaxy NGC 4374 are due to both the abundances falling with galaxy radius and the large effective apertures. Alternately, the lower masses of the cooler gas galaxies, compared to the hot, bright ellipticals, may not have been sufficient to blind the heavy-element enriched gas generated in the early epochs. More of this enriched gas may have been contained in deeper, more extensive potentials, such as those around NGC 1399 and NGC 4472.

The models presented in David, Forman, & Jones (1991) show that the fraction of iron synthesized by stars that is ejected in a galactic wind depends on the galaxy mass, the stellar initial mass function, the star formation rate, and the history of type Ia supernovae. For example, in the set of models with a Salpeter IMF, a present-epoch type Ia supernova rate equal to one-fourth of Tammann's (1974) value, and a star formation rate that declines on a timescale of 10^8 years, the galaxy model with $L_B = 10^{11}\ L_\odot$ retains twice as much iron (per stellar mass) as the galaxy model with $L_B = 10^{10}\ L_\odot$. This increase in iron retention with increasing galaxy luminosity (or mass) is consistent with the observed trend.

Although the *ROSAT* X-ray spectra of the Fornax galaxies are well-described by single spectra, the suggestion of a possible second spectral component was made by Fabbiano, Kim, & Trinchieri (1994) for the two Virgo galaxies NGC 4365 and NGC 4382. We analyzed the *ROSAT* observations of these galaxies and found their spectra to be well fitted (χ^2 values of 9 to 16 for 25 spectral bins) by single thermal spectra with low abundances. The results are given in Table 4 and are comparable to those found for the Fornax galaxies. The determination by *ASCA* of low abun-

TABLE 4

SPECTRAL PARAMETERS FOR LOW-LUMINOSITY GALAXIES IN FORNAX AND VIRGO

Galaxy	kT (keV) or α	Range	n_H	Range	Fe Abundance	Range
68% Confidence Ranges on Fitted Parameters						
NGC 1379......	0.55	0.29–1.71	1.04	0.00–3.05	0.05	0.0–0.28
NGC 1380......	2.91	2.48–3.37	4.20	2.90–5.64	...	...
NGC 1381......	0.79	0.37–2.35	0.78	0.19–1.58	...	...
NGC 1387......	0.54	0.46–0.62	2.11	0.86–3.23	0.15	0.08–0.43
NGC 1404......	0.65	0.63–0.66	2.02	1.82–2.22	0.16	0.14–0.19
NGC 4365......	0.75	0.51–1.37	2.06	1.48–2.77	0.01	0.00–0.06
NGC 4382......	0.46	0.37–0.58	3.17	2.08–4.36	0.03	0.01–0.10

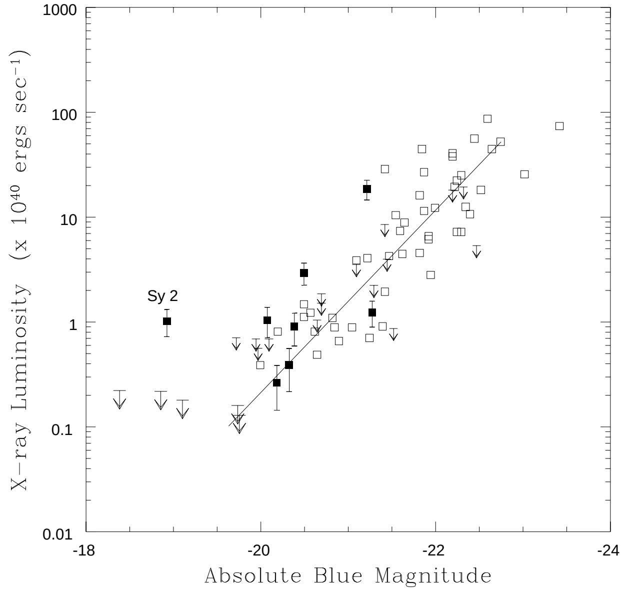

FIG. 9.—For the 13 Fornax galaxies (excluding NGC 1399) observed with the PSPC, we show, with solid symbols or X-ray upper limits, their absolute blue magnitudes plotted against their 0.5–4.5 keV X-ray luminosities. We also show a sample of early-type galaxies observed with *Einstein* that have well determined distances (Donnelly et al. 1990). The luminosities for the Fornax galaxies were computed in the energy band 0.5–4.5 keV for the distance of 27.5 Mpc used by Donnelly et al. for the Fornax cluster. The line is the best-fit relation of X-ray luminosity and optical magnitude determined by Donnelly et al. for the *Einstein* sample. NGC 1427A is a Seyfert 2 galaxy and falls well above the correlation of absolute magnitude and X-ray luminosity found for early-type galaxies.

dances in the Fornax galaxy NGC 1404 and the Virgo galaxy NGC 4374 strongly supports the idea that the spectra of these galaxies arise primarily from thermal gas with a low abundance of iron.

To determine the 0.2 to 2.0 keV X-ray fluxes for these galaxies from the counting rates, we used a conversion of 1 PSPC count s^{-1} to 9.2×10^{-12} ergs cm^{-2} s^{-1}. This conversion is appropriate for the elliptical galaxies in Fornax, whose X-ray emission is primarily thermal with gas temperatures from 0.5 to 1.3 keV. For NGC 1380, whose X-ray emission appears pointlike, the appropriate conversion for the fitted spectrum is 8.5×10^{-12} ergs cm^{-2} s^{-1}. The X-ray luminosities of these galaxies range from 10^{39} ergs s^{-1} to 1.6×10^{41} ergs s^{-1}. The galaxy absolute magnitudes are plotted against their X-ray luminosities in Figure 9. We also show the early-type galaxies with well-determined distances from Donnelly, Faber, & O'Connell (1990). The solid line shows the relationship for samples of elliptical and S0 galaxies derived from *Einstein* observations (e.g., Forman et al. 1985, Donnelly et al. 1990). Although the correlation of the optical magnitude and the X-ray luminosity for the early-type Fornax galaxies appears to be steeper than found previously, the apparent steepness can be attributed to NGC 1404, which is brighter in X-rays than average for its optical magnitude. Moreover, the Fornax galaxies all fall within the envelope of emission defined by the larger *Einstein* sample. We suggest that the steepness of this relation for Fornax galaxies is probably due to the relatively small number of galaxies in the sample. Thus we confirm earlier results (e.g., Donnelly et al.) that the dispersion in the magnitude/X-ray luminosity relation is not due solely to distance errors, but is related to either intrinsic differences in the galaxies or, more likely, to differences in their local environment.

The spectral results on the Fornax galaxies, as well as their extension of the correlation of X-ray luminosity and optical magnitude, supports the idea that their emission originates predominantly from hot gas. We can also use the detection of X-ray point sources in Cen A (Ruiz, Jones, & Forman 1997) to predict their contribution to the X-ray emission of Fornax galaxies, if the Cen A sources are typical of the point source population in other elliptical galaxies. We find for the faint Fornax galaxies ($M_B = -19.8$ to -20.2), where this contribution is expected to be the largest, that the predicted point source contribution ranges from 3% to 30% of the measured X-ray flux.

Figure 10 shows the X-ray intensity contours for NGC 1404 superposed on the optical image. The lower-luminosity contours are elongated toward the southeast. The higher-resolution *ROSAT* HRI images show that this extension is not due to a second point source. The asymmetry in the emission around NGC 1404, while less pronounced than the trail of X-ray emission from the Virgo galaxy M86 (NGC 4406) (Forman et al. 1979; White et al. 1991), indicates that the hot gas corona around the galaxy is being stripped by ram pressure as the galaxy (apparently) falls toward NGC 1399 and the high gas density in the center of the Fornax cluster.

In our analysis, we used a distance modulus of 31.9 for Fornax, corresponding to a distance of 24 Mpc. For Fornax, smaller distances have often been used by others, including Bicknell et al. (1989) and Grillmair et al. (1994), who used a distance of 13.35 Mpc (a distance modulus of 30.6). If we used the smaller distance, the optical magnitudes for several early-type galaxies for which we observe extended X-ray emission would be fainter than -18.8. These include three for which we measure a gas temperature of about 0.5 keV (NGC 1379, NGC 1381, and NGC 1387). For a distance of 13.35 Mpc, only the Fornax ellipticals NGC 1404 and NGC 1399 would have absolute magnitudes brighter than -19.5.

Based on simulations, David et al. (1990) found that galaxies fainter than about -20 should have partial winds, while those fainter than -19 should have subsonic winds. These faint galaxies should not have detectable hot coronae. Since we observe 0.5 keV coronae around several early-type Fornax galaxies, their absolute magnitudes should exceed -19, which requires that the distance to Fornax exceed 18 Mpc (and, if there are not large peculiar velocities, that the Hubble constant be less than about 75 s km^{-1} s^{-1} Mpc^{-1}). This lower limit on the distance to Fornax is consistent with the 16.9 ± 1.1 Mpc distance determined by McMillan, Ciardullo, & Jacoby (1993) from analysis of the planetary nebula luminosity function.

7. SUMMARY

The presence of hot gas in nearly hydrostatic equilibrium in the halos of elliptical galaxies allows the total mass and its distribution to be measured. Since this corona of hot gas also is the repository of recent mass loss from the galaxy, its study also determines the enrichment history of the galaxy. The good spatial resolution, large field of view, low background, and well-calibrated energy scale of the *ROSAT* PSPC have permitted a detailed study of the X-ray emission associated with the Fornax cluster. Our study included both the emission that can be associated with individual

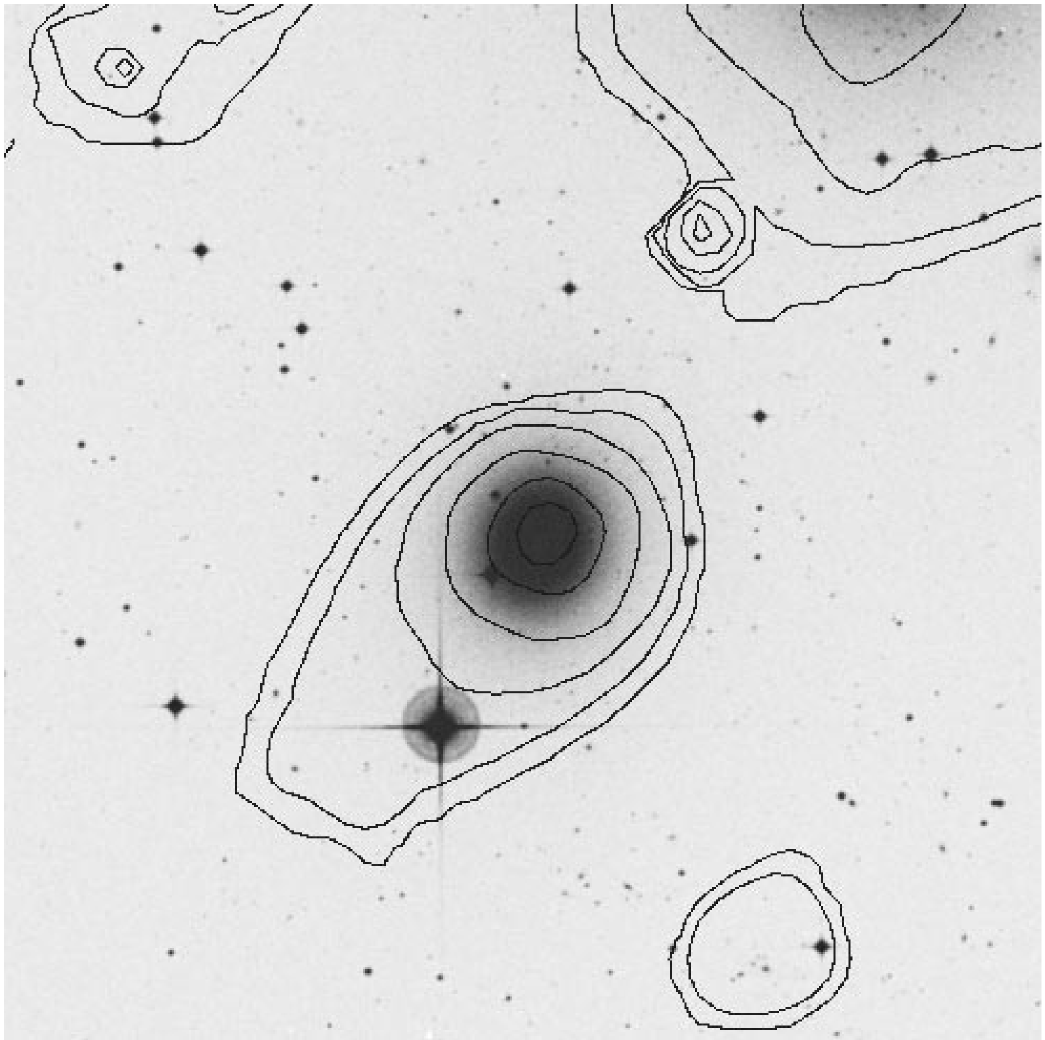

FIG. 10.—X-ray isointensity contours for NGC 1404, derived from a wavelet analysis (Vikhlinin et al. 1996), superposed on the optical image. The extension of the X-ray emission to the southeast is not due to emission from a point source (as confirmed by our examination of a deep *ROSAT* HRI image), but probably results from the ram pressure stripping of the hot corona around NGC 1404 as it falls toward the central, denser region around NGC 1399.

galaxies and that which is centered on NGC 1399, but which, like the X-ray emission from M87 in Virgo, probably owes its extent to the position of the galaxy near the center of the larger cluster potential.

The primary results of this study are:

1. The dark halo around NGC 1399 has a mass-to-light ratio comparable to that found in groups and clusters of galaxies.

2. A comparison of NGC 1399 and the Fornax cluster with M87 and the Virgo cluster suggests that, following the formation of similar galaxies at their centers, these two systems had different formation histories, probably due to differences in their local density perturbations.

3. Like the heavy element abundances measured in NGC 4472, the abundances in the gas around NGC 1399 require a low rate for type Ia supernovae, with little evolution in that rate over time.

4. The X-ray surface brightness isophotes and location of the optical galaxy imply that the NGC 1399 galaxy is not at rest within the dark matter halo.

We thank the referee for useful comments. This work is supported by the Smithsonian Astrophysical Observatory and NASA contracts and grants NAS 8-39073 and NAG 8-1536.

REFERENCES

Bahcall, J., & Sarazin, C. 1977, ApJ, 213, L99
Bicknell, G., Bruce, T., Carter, D., & Killeen, N. 1989, ApJ, 336, 639
Bridges, T., Hanes, D., & Harris, W. 1991, AJ, 101, 469
Cappellaro, E., Tunatto, M., Benetti, S., Tsvetkov, D., Bartunov, O., & Makarova, I. 1993, A&A, 273, 383
Ciotti, L., D'Ercole, A., Pellegrini, S., & Renzini, A. 1991, ApJ, 376, 380
David, L., Forman, W., & Jones, C. 1990, ApJ, 359, 29
———. 1991, ApJ, 380, 39
David, L., Jones, C., & Forman, W. 1995, ApJ, 445, 578
David, L., Jones, C., Forman, W., & Daines, S. 1994, ApJ, 428, 544
D'Ercole, A., Renzini, A., Ciotti, L., & Pellegrini, S. 1989, ApJ, 341, L9
de Vaucouleurs, G., & de Vaucouleurs, A. 1964, Reference Catalogue of Bright Galaxies (Austin: Univ. Texas Press)
de Vaucouleurs, G., de Vaucouleurs, A., & Corwin, H. G. 1976, Second Reference Catalogue of Bright Galaxies (Austin: Univ. Texas Press)
Donnelly, R., Faber, S., & O'Connell, R. 1990, ApJ, 354, 52
Fabbiano, G., Kim, D.-W., & Trinchieri, G. 1994, ApJ, 429, 94
Fabian, A. C. 1994, ARA&A, 32, 277
Fabian, A., Nulsen, P., & Canizares, C. 1984, Nature, 310, 733
———. 1991, A&A Rev., 2, 191

Fabian, A., Thomas, P., Fall, M., & White, R. 1986, MNRAS, 221, 1049
Fabricant, D., & Gorenstein, P. 1983, ApJ, 267, 535
Fabricant, D., Lecar, M., & Gorenstein, P. 1980, ApJ, 241, 552
Ferguson, H. 1989, A&A, 111, 222
Forman, W., Jones, C., David, L., Franx, M., Makishima, K., & Ohashi, T. 1993, ApJ, 418, L55
Forman, W., Jones, C., & Tucker, W. 1985, ApJ, 293, 102
Forman, W., Schwarz, J., Jones, C., Liller, W., & Fabian, A. 1979, ApJ, 234, L27
Franx, M. 1988, Ph.D. thesis, Univ. Leiden
Grillmair, C., Freeman, K., Bicknell, G., Carter, D., Couch, W., Sommer-Larson, J., & Taylow, K. 1994, ApJ, 422, L9
Hanes, D., & Harris, W. 1986, ApJ, 309, 564
Ikebe, Y., et al. 1992, ApJ, 384, L5
———. 1996, Nature, 379, 427
Jones, C., & Forman, W. 1984, ApJ, 276, 38
———. 1994, in AIP Conf. Proc. 313, The Soft X-ray Cosmos ed. E. Schlegel & R. Petre (New York: AIP), 129
Killeen, N., & Bicknell, G. 1988, ApJ, 325, 165
Loewenstein, M., & Mathews, W. 1987, ApJ, 319, 614
———. 1991, ApJ, 373, 445
Loewenstein, M., Mushotzky, R., Tamura, T., Ikebe, Y., Makishima, K., Matsushita, K., Awaki, H., & Serlemitsos, P. 1994, ApJ, 436, L75
Mason, K. O., & Rosen, S. R. 1985, Space Sci. Rev., 40, 675
Mathews, W. 1978, ApJ, 219, 413
Matilsky, T., Jones, C., & Forman, W. 1985, ApJ, 291, 621
McMillan, R., Ciardullo, R., & Jacoby, G. 1993, ApJ, 416, 62
Mushotzky, R., Loewenstein, M., Awaki, H., Makishima, K., Matsushita, K., & Matsumoto, H. 1994, ApJ, 436, L79
Rangarajan, V., Fabian, A. C., Forman, W., & Jones, C. 1995, MNRAS, 272, 665
Ruiz, S., Jones, C., & Forman, W. 1997, ApJ, submitted
Sandage, A., & Tammann, G. 1981, A Revised Shapley-Ames Catalog of Bright Galaxies (Washington: Carnegie Institution of Washington)
Schombert, J. M. 1986, ApJS, 60, 603
Serlemitsos, P., Loewenstein, M., Mushotzky, R., Marshall, F., & Petre, R. 1993, ApJ, 413, 518
Snowden, S., Plucinsky, P., Briel, U., Hasinger, G., & Pfeffermann, E. 1992, ApJ, 393, 819
Stark, A., Gammie, C., Wilson, R., Bally, J., Linke, R., Heiles, C., & Hurwitz, M. 1992, ApJS, 79, 77
Sulentic, J., & Tifft, W. 1973, The Revised New General Catalogue of Nonstellar Astronomical Objects (Tucson: Univ. Arizona Press)
Tammann, G. 1974, in Supernovae and their Remnants, ed. Cosmovici (Dordrecht: Reidel)
Thomas, P., Fabian, A., Arnaud, K., Forman, W., & Jones, C. 1986, MNRAS, 222, 655
van den Bergh, S., & Tammann, G. 1991, ARA&A, 29, 363
Vikhlinin, A., Forman, W., & Jones, C. 1996, ApJ, 474, L7
White, D., Fabian, A. C., Forman, W., Jones, C., & Stern, C. 1991, ApJ, 375, 35
Worthey, G., Faber, S., & Jesus Gonzalez, J. 1992, ApJ, 398, 69